

Statistical and Physical Analysis of the Vertical Structure of Precipitation in the Mountainous West Region of the United States Using 11+ Years of Spaceborne Observations from TRMM Precipitation Radar

QING CAO

*Advanced Radar Research Center, University of Oklahoma, and Hydrometeorology and Remote Sensing Laboratory,
National Weather Center, Norman, Oklahoma*

YANG HONG

*Advanced Radar Research Center, University of Oklahoma, and Hydrometeorology and Remote Sensing Laboratory,
National Weather Center, and School of Civil Engineering and Environmental Sciences, University of Oklahoma,
Norman, Oklahoma*

JONATHAN J. GOURLEY, YOU CUN QI, AND JIAN ZHANG

NOAA/National Severe Storms Laboratory, Norman, Oklahoma

YIXIN WEN

*Advanced Radar Research Center, University of Oklahoma, and Hydrometeorology and Remote Sensing Laboratory,
National Weather Center, Norman, Oklahoma*

PIERRE-EMMANUEL KIRSTETTER

*Hydrometeorology and Remote Sensing Laboratory, National Weather Center, and NOAA/National Severe Storms Laboratory,
Norman, Oklahoma*

(Manuscript received 2 April 2012, in final form 27 July 2012)

ABSTRACT

This study presents a statistical analysis of the vertical structure of precipitation measured by NASA–Japan Aerospace Exploration Agency’s (JAXA) Tropical Rainfall Measuring Mission (TRMM) precipitation radar (PR) in the region of southern California, Arizona, and western New Mexico, where the ground-based Next-Generation Radar (NEXRAD) network finds difficulties in accurately measuring surface precipitation because of beam blockages by complex terrain. This study has applied TRMM PR version-7 products 2A23 and 2A25 from 1 January 2000 to 26 October 2011. The seasonal, spatial, intensity-related, and type-related variabilities are characterized for the PR vertical profile of reflectivity (VPR) as well as the heights of storm, freezing level, and bright band. The intensification and weakening of reflectivity at low levels in the VPR are studied through fitting physically based VPR slopes. Major findings include the following: precipitation type is the most significant factor determining the characteristics of VPRs, the shape of VPRs also influences the intensity of surface rainfall rates, the characteristics of VPRs have a seasonal dependence with strong similarities between the spring and autumn months, and the spatial variation of VPR characteristics suggests that the underlying terrain has an impact on the vertical structure. The comprehensive statistical and physical analysis strengthens the understanding of the vertical structure of precipitation and advocates for the approach of VPR correction to improve surface precipitation estimation in complex terrain.

1. Introduction

Modern ground-based weather radar, capable of providing atmosphere surveillance with high temporal (several minutes) and spatial (<1 km) resolution, is essential

Corresponding author address: Dr. Yang Hong, Hydrometeorology and Remote Sensing Laboratory and Advanced Radar Research Center, 120 David L. Boren Blvd., Suite 4610, Norman, OK 73072.
E-mail: yanghong@ou.edu

for weather-related applications for natural hazard detection and warning. The Next Generation Radar (NEXRAD) network, which consists of 159 S-band (10 cm) Weather Surveillance Radar-1988 Doppler (WSR-88D) radars and covers the continental United States (CONUS), is the major facility of National Oceanic and Atmospheric Administration's (NOAA) National Weather Service (NWS) that provides information for severe weather detection–warning, quantitative precipitation estimation (QPE), quantitative precipitation forecasts (QPF), and flash flood warning–forecast. Recently an advanced QPE system based on the NEXRAD, NOAA's Next Generation National Mosaic and QPE System (NMQ; <http://nmq.ou.edu>), has been developed by researchers at NOAA's National Severe Storms Laboratory (NSSL) and the University of Oklahoma (OU). With advanced techniques of quality control (Lakshmanan et al. 2007), data mosaicking (Zhang et al. 2005), and rainfall estimation (Vasiloff et al. 2007), the NMQ system is capable of generating high quality of QPE in real time over the CONUS (Zhang et al. 2011). However, NEXRAD observations have some intrinsic limitations (Maddox et al. 2002), which consequently degrade the quality of QPE products. In mountainous regions, radar beams can be blocked (or partially blocked) by the surrounding terrain. In such a case measurements are available only from higher elevation angles that scan higher levels of the atmosphere. The ascending and broadening of the beam can also lead to partial or complete overshooting of the cloud top at far range. In these situations, use of high-level measurements can result in considerable bias when they are used to estimate surface precipitation. Corrections should be made for more accurate precipitation estimation.

The vertical profile of reflectivity (VPR), which reveals the vertical structure of a storm, links the surface precipitation to the radar observation at higher levels. As a result, a great deal of research has been conducted on the utilization of VPR information for improving surface rainfall estimation (Kitchen et al. 1994; Fabry and Zawadzki 1995; Vignal et al. 2000; Germann and Joss 2002; Bellon et al. 2005; Zhang and Qi 2010). In mountainous regions (e.g., the analysis region of this study) where radar measurements near the surface are less ubiquitous, knowledge of the VPR is particularly useful for accurately estimating surface rainfall (Germann and Joss 2002; Kirstetter et al. 2010). High-resolution and representative VPRs are not readily obtained from ground-based radar (e.g., NEXRAD) observations due to blockages and high spatial variability of vertical precipitation structure. It has been realized that spaceborne radars can be utilized to improve ground-based radar observations, for example, compensating the range

degradation of ground-based radar (Gabella et al. 2011). Although their measurements near the surface are affected by ground clutter as well, spaceborne radars have great advantages in measuring the vertical structure of storms because their measurements are much less impacted by intervening mountain blockages and beam broadening effects in the vertical direction (Kummerow et al. 2000). Their vertical resolution is usually higher than that of ground-based radar (e.g., NEXRAD), especially at far ranges (e.g., >100 km). Spaceborne radar thus offers major advantages as a tool to investigate storm's VPR characteristics, ultimately leading to improved precipitation estimates in mountainous regions.

The purpose of this study is to analyze the vertical structure of precipitation in the region of southern California, Arizona, and western New Mexico, where ground-based NEXRAD radars find difficulties in accurately measuring surface precipitation because of the complex terrain (as shown in Figs. 1a,b). To achieve the goal, spaceborne radar observations from Tropical Rainfall Measuring Mission (TRMM), the world's foremost satellite specifically designed for precipitation measurement and managed jointly by National Aeronautics and Space Administration (NASA) and Japan Aerospace Exploration Agency (JAXA), are used for the analysis. The TRMM satellite carries the first spaceborne weather radar, called precipitation radar (PR), which operates at Ku band with a frequency of 13.8 GHz (Kozu et al. 2001; Kummerow et al. 2000). PR scans across a 215-km-wide footprint, with vertical and horizontal resolutions of 250 m and 4.3 km, respectively, at nadir. Considering that precipitating systems typically extend several kilometers in the vertical direction, PR's vertical resolution of 250 m ensures fine observation suitable for studying the vertical structures of storms. Many previous works have investigated the vertical structure of storms using observations from TRMM PR. Particularly, those studies using long-term statistics of PR data have focused on the spatial and/or temporal variation of vertical profile of rainfall and/or radar reflectivity for a given analysis region (e.g., Shin et al. 2000; Hirose and Nakamura 2002, 2004; Geerts and Dejene 2005; Williams et al. 2007). However, few efforts have been put into the study of a mountainous region and the attempt of using PR-derived VPR to enhance the ground radar QPE. In this study, a statistical analysis of PR observations reveals the seasonal, spatial, intensity- and type-related variations of VPR characteristics in the analysis region, which will be very valuable information for improving ground radar QPE in mountainous regions. The current study focuses on the understanding of the vertical structure of storms and the climatological characteristics of the VPR, and future studies will focus on the application of the VPR characteristics for correcting

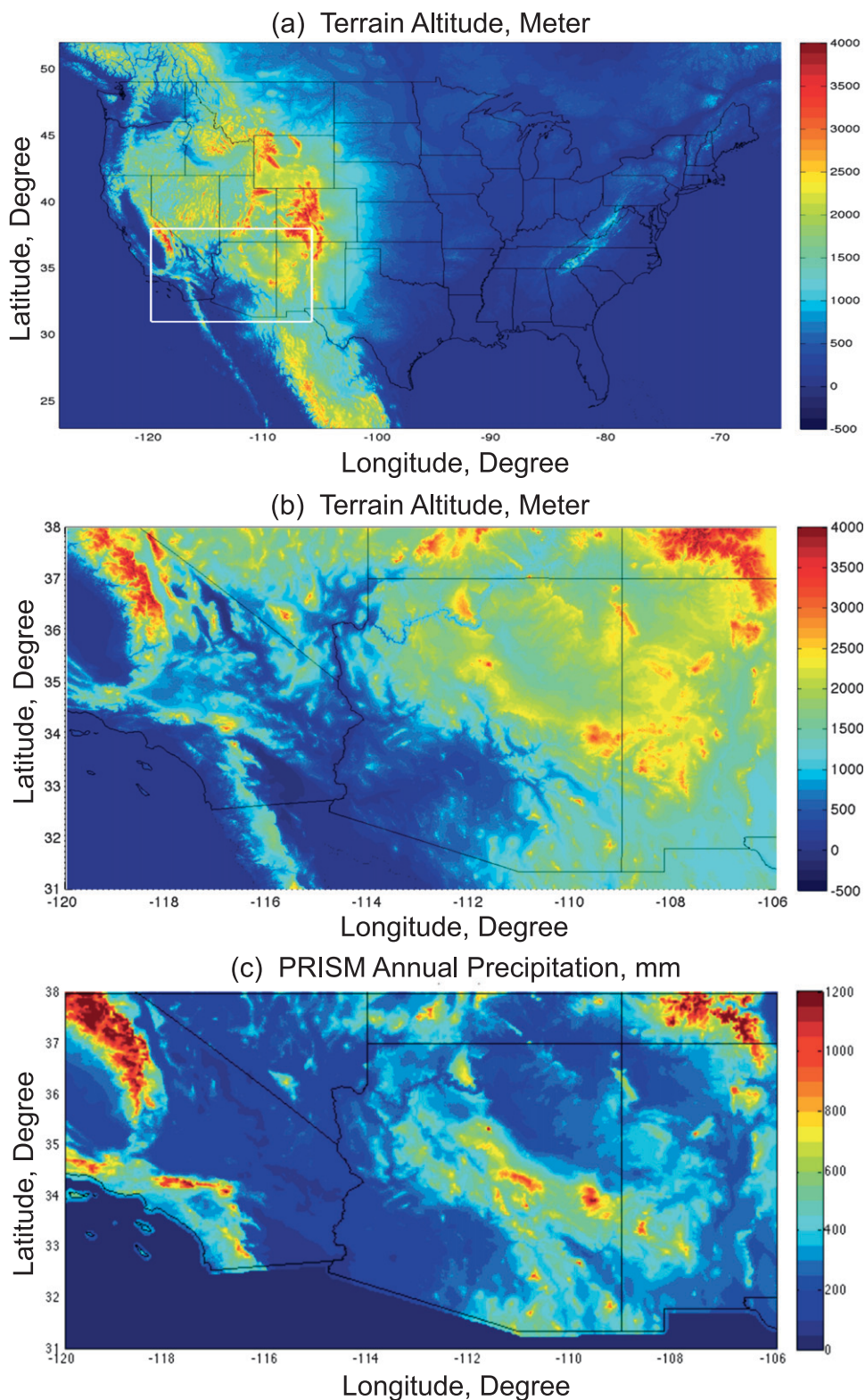


TABLE 1. TRMM V7 data (2A23, 2A25) availability by month, where 1 indicates January, 2 indicates February, etc.

	1	2	3	4	5	6	7	8	9	10	11	12	Total
Rain events	148	161	166	117	85	65	198	247	167	149	100	148	1751
Observed events	71	74	68	47	42	38	125	143	87	74	43	67	879
PR passes with rain	216	271	224	137	107	125	531	609	329	248	130	196	3123

radar QPEs in real time. The remainder of this paper is organized as follows. The TRMM datasets used for the analysis are described in section 2. Section 3 presents detailed statistics of TRMM data and the VPR analysis. Considerations for VPR correction are discussed in section 4. The last section provides the conclusions, summarizing remarks, and future directions.

2. Dataset

For the past 10 years, much effort from scientists in the United States, Japan, and other countries has been put into generating state-of-the-art radar-precipitation products with TRMM PR (e.g., Meneghini et al. 2000, 2004; Iguchi et al. 2000, 2009; Schumacher and Houze 2003; Takahashi and Iguchi 2004; Seto and Iguchi 2007; Awaka et al. 2009). There are three levels of radar algorithms for TRMM PR products. Level 1 algorithms calculate basic radar parameters such as return power and radar reflectivity Z . These algorithms also deal with data quality control and calibration. Level 2 algorithms generate the products associated with the radar signal processing and the physical processes of storms. Level 3 algorithms perform the space-time averaging and statistics of level 1 and level 2 products. The datasets used for the current study were generated by two level 2 algorithms: PR qualitative algorithm (2A23) and PR profile algorithm (2A25). 2A23 data include products for brightband detection and quantification, and precipitation type classification (Awaka et al. 2007, 2009). 2A25 data provide range profiles of attenuation-corrected radar reflectivity and corresponding rainfall estimation (Meneghini et al. 2000, 2004; Iguchi et al. 2000, 2009).

The TRMM science team has released several versions of data-processing algorithms since the launch of TRMM satellite in 1997. The latest version of TRMM algorithms, version 7 (TRMM V7), was released in September 2011 (TRMM Precipitation Radar Team 2011). Compared to the version 6 released in 2004, TRMM V7 have introduced improvements (e.g., Seto and Iguchi 2007; Awaka et al. 2009; Iguchi et al. 2009). For example, the 2A23 algorithm now better detects the bright band and shallow storms. It has also increased the rain type subcategories and refines the classification. The 2A25 algorithm produces enhanced radar reflectivity profiles by improving path-integrated attenuation (PIA) estimation and refining the

attenuation correction method. Rain estimation is now improved with the introduction of a new drop size distribution (DSD) model. Nonuniform beam filling (NUBF) correction was also reintroduced in V7.

The current study examines TRMM PR V7 data for time span of more than 11 years, from 1 January 2000 to 26 October 2011. According to the surface rain gauge measurements, the total number of rainy days in the analysis region is 1751. However, because of the mismatch of time and space between the PR scan and the evolution of storms, PR observed 879 events, where an event is defined by the summation of PR's rainfall rate product in the analysis region greater than 10 mm h^{-1} . The total number of passes over the analysis domain during rainy events is 3123, or 3.6 passes on average for each event. Additional details about the data availability are provided in Table 1. The monthly analysis indicates there are many fewer precipitation events occurring in May and June than in July and August, which is attributed to the onset of the North American monsoon. The average number of precipitating days in the Intermountain West and the adjacent coastal region is less than 6 days in June and about 21 days in August.

Figure 2 illustrates the spatial pattern of satellite overpasses and precipitation, which is further analyzed in the rest of the paper. PR scans are concentrated on the latitude band from 34° to 35°N , for which the maximum number of overpasses is approximately 1500. There is no observation beyond 36.3°N . PR observed the region from 31° to 32°N with approximately 500 overpasses. Figure 2b shows the total accumulated precipitation calculated from the datasets, which generally agrees with the PRISM precipitation climatology shown in Fig. 1c except for a dearth of precipitation in southern California (about 36°N , 118.5°W) according to TRMM PR. The maximum precipitation is observed across central Arizona, where the elevation is generally greater than 1000 m and rises very quickly from southwest to northeast (Fig. 1b). The region where the altitude is below 500 m generally has less precipitation. For example, in the low deserts of California and southwest Arizona, the observed total precipitation is mostly less than 600 mm and much less than in higher-altitude regions that were scanned by PR with at a similar frequency (i.e., have similar number of PR overpasses according to Fig. 2a).

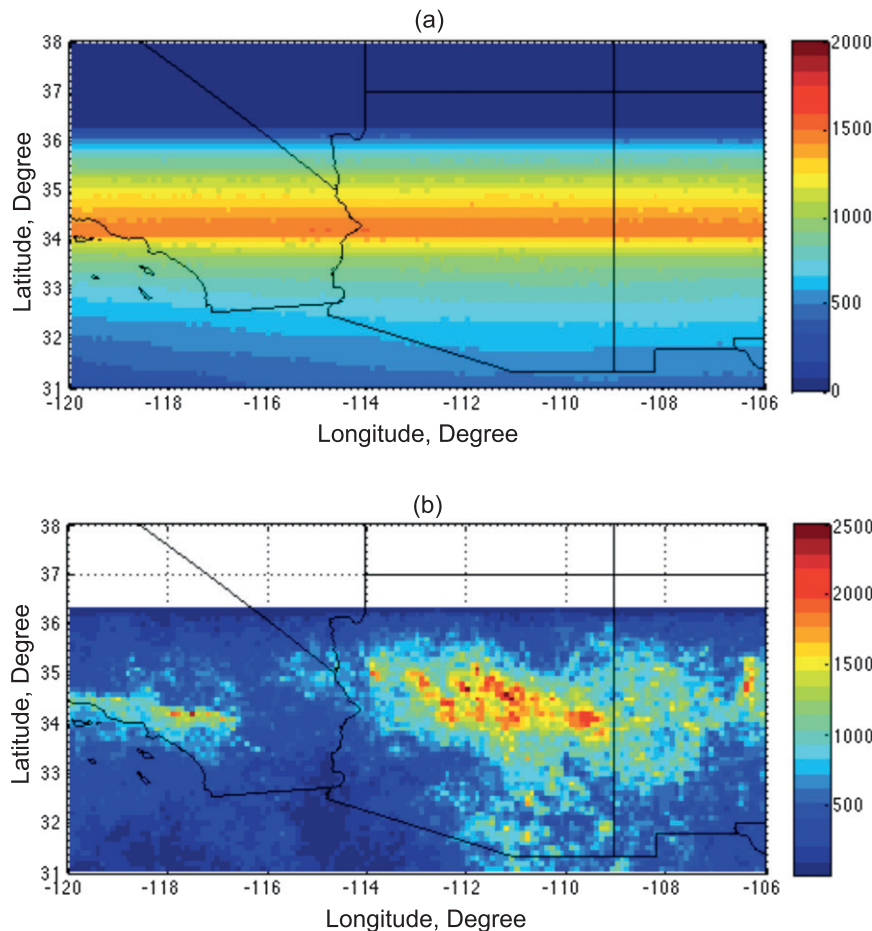


FIG. 2. Statistics of TRMM PR dataset used for analysis: (a) the total pass number of PR scans with precipitation observed over the analysis region; (b) the total precipitation measured by the PR. The calculation has assumed 1-h accumulation with the rainfall rate measured by PR and is the summation of all the 1-h precipitation. The spatial resolution is $0.1^\circ \times 0.1^\circ$.

Based on algorithms proposed by Awaka et al. (2007, 2009) and Steiner et al. (1995), V7 of 2A25 applies more than 30 subcategories for the classification of rain types. Those subcategories can be summarized with several major types: “stratiform,” “stratiform maybe,” “convective,” “convective maybe,” and “others.” The stratiform type will be identified when the bright band (BB) is clearly detected and the VPR reveals apparent features of stratiform precipitation. When the BB does not exist and the VPR reveals convective characteristics, the precipitation will be classified with the convective type. When the BB is not clearly detected the precipitation will be assigned as either convective maybe or stratiform maybe, with the latter distinction being tied to the precipitation structure. Hereafter, we have combined the convective maybe type into the convective type for the data analysis.

Climatological VPRs for stratiform, convective, and stratiform maybe are presented in Fig. 3. The occurrence frequency is calculated using 0.1-dB and 250-m intervals

for reflectivity and altitude, respectively. The calculation of percentile curves has considered the valid data points only. That is to say, given a 250-m bin, only VPRs with valid reflectivity (excluding no/bad values) have been used for the percentile calculation. The total number of VPRs for stratiform, convective, and stratiform maybe are 332 165, 314 482, and 1 094 950, respectively. The larger number of stratiform maybe types implies that most stratiform precipitation structures in the region do not have a strong BB signature. The maximum reflectivity of stratiform maybe VPRs is typically less than 30 dBZ, which means the precipitation is quite weak and the BB is less likely to be detected by PR. This inference is supported by the percentile curves in Fig. 3a, which show the BB feature becomes more prominent and detectable for VPRs with increasing percentile. It is also noted that the intensity of the BB is less than 34 dBZ for about 90% of the stratiform VPRs while about 40% of the convective VPRs have a maximum reflectivity more

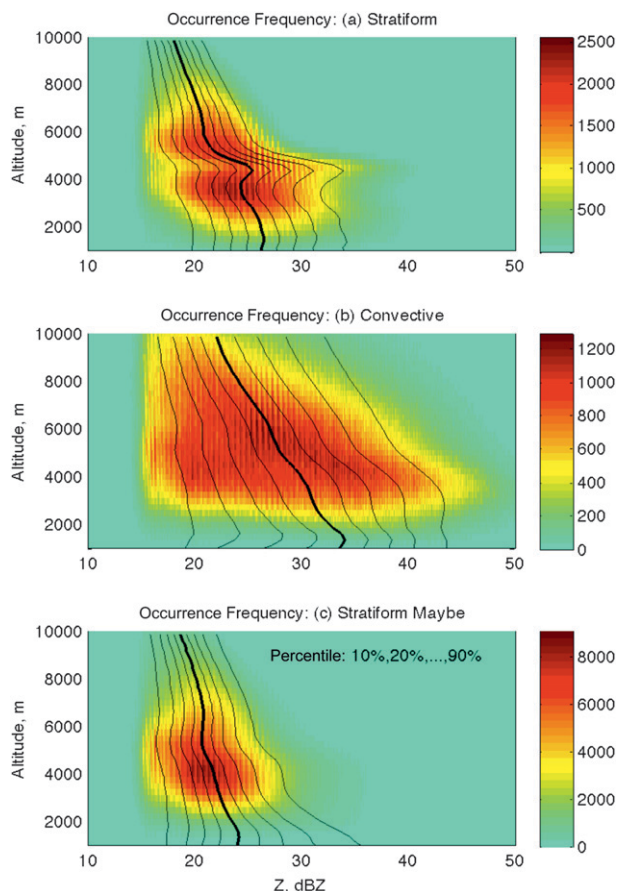


FIG. 3. Vertical profile (in meters above mean sea level) of occurrence frequency of radar reflectivity for whole PR dataset: (a) stratiform, (b) convective, and (c) stratiform maybe precipitation. Nine solid lines indicate the 10–90 percentiles with an interval of 10%. The thick solid line represents the 50-percentile curve. For the calculation of occurrence frequency, the intervals of Z and altitude are set to be 0.1 dB and 250 m, respectively.

than 34 dBZ. Caution should be exercised when interpreting the slopes of the percentile curves in regions with low data densities. For example, percentile calculations at low altitudes (e.g., <2000 m) may not be reliable. Ground clutter and signal attenuation could affect the validity of measurements close to the surface. Most of the profiles shown in Fig. 3 do not have valid attenuation-corrected reflectivity below a height of 2 km, presumably because of terrain effects. Detailed analyses of VPR data are provided in the next section.

3. Analysis results

a. Vertical profile of radar reflectivity

Beyond revealing the vertical structure of storms, the VPR also reveals microphysical processes. For example, stratiform precipitation often has a distinct radar BB

feature around the freezing level (0°C level), which can be discerned from their VPRs. The BB can be a good indicator of the level at which hydrometeors change phase. Above the BB, the phase of hydrometeors is likely dry ice or snow while it is predominantly liquid below the BB. Within the BB layer itself, there exists mixed-phase hydrometeors including melting ice–snow and raindrops. The information provided by VPR analysis facilitates the investigation of microphysical processes and the quantitative retrieval of liquid water content of precipitation.

Seasonal VPR variations are revealed in Figs. 4–6. PR data collected in spring (March, April, May), summer (June, July, August), autumn (September, October, November), and winter (December, January, February) have been processed and composited separately. Considering that surface rainfall of different intensities may be related to different VPR features, the PR data have also been sorted into 24 categories with surface rainfall rate varying from 0.4 to 80 mm h^{-1} . The mean VPR is created with VPRs having the surface rainfall rate with a 20% variation. For example, VPRs with rainfall rates $8\text{--}12\text{ mm h}^{-1}$ are sorted and averaged to obtain representative VPR of 10 mm h^{-1} . To reduce the dominant effect of high reflectivity values, the calculation of mean VPR is in the logarithm domain (dBZ). The dashed line on the right side of each figure panel gives the mean standard deviation of calculation of each representative mean VPR. Most standard deviation values are 2–3 dB, showing good similarity of Z values for VPRs with similar surface rainfall rates. Several mean VPRs might be missing for high rainfall rates (e.g., VPRs for 30, 40, and 80 mm h^{-1} are missing for summer stratiform precipitation) because of the lack of sufficient observations. Recalling the distribution of data points shown in Fig. 3, it is obvious that most of VPRs are associated with moderate or light precipitation (e.g., more than 90% of VPRs have surface rainfall rate less than 5 mm h^{-1}).

Among the four seasons, summer results show the most evident BB features, even for VPRs with light precipitation. As shown in Fig. 4b, the reflectivity difference from the BB peak to the raining region below tends to increase for weaker precipitation, consistent with the study of Fabry and Zawadzki (1995). This difference is about 2 dB for moderate rain ($2.5\text{--}10\text{ mm h}^{-1}$) but reaches 4 dB for very light rain ($<0.5\text{ mm h}^{-1}$). The BB features are not as obvious in the mean VPRs of the other three seasons. This result suggests that the height of the BB has more variation during these three seasons, and the BB feature has been smoothed in the mean VPR curves. The mean height of the BB during summer is approximately 2 km higher than during the other three

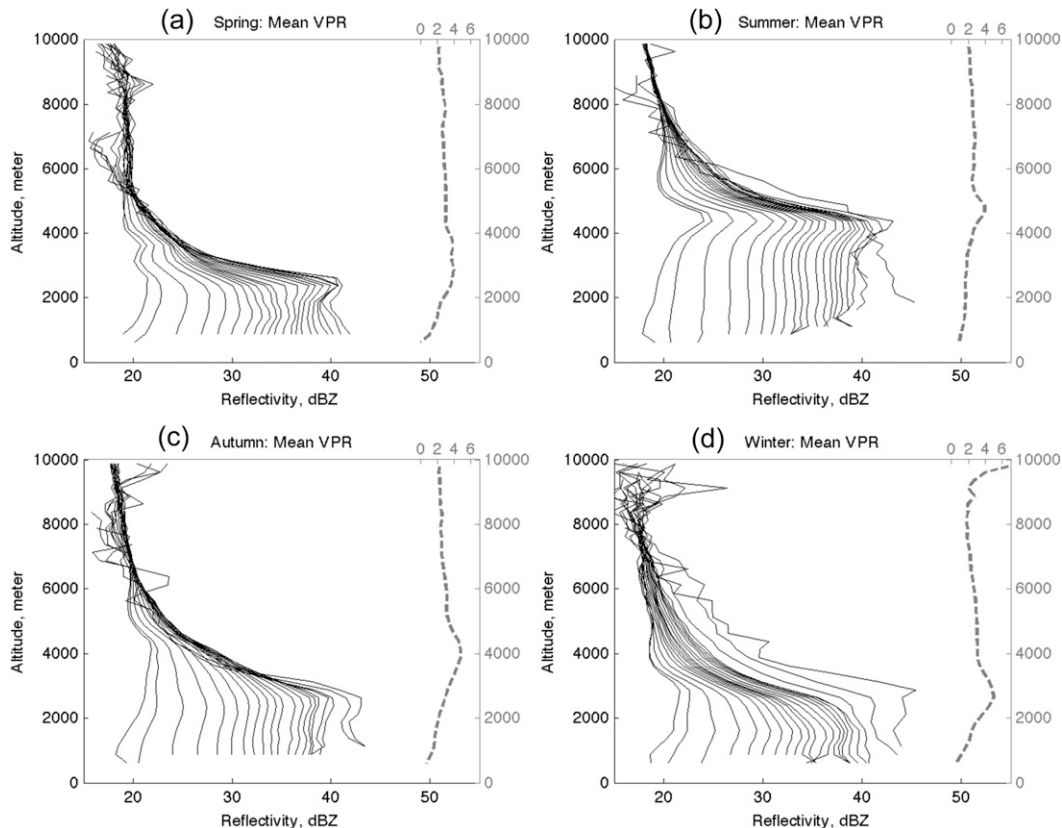


FIG. 4. Seasonal variation of VPR for the type of stratiform precipitation: (a) spring, (b) summer, (c) autumn, and (d) winter. Solid lines represent the mean curves of VPRs, which are categorized from left to right by the surface rainfall rates (mm h^{-1}): 0.4, 0.6, 1, 1.5, 2.0, 2.5, 3.0, 3.5, 4.0, 4.5, 5.0, 6.0, 7.0, 8.0, 9.0, 10.0, 12.0, 15.0, 20.0, 25.0, 30.0, 40.0, 60.0, and 80.0, respectively. The variation of surface rainfall rate is set to 20% for the calculation of mean VPR. Dashed line gives the mean value of standard deviations of each mean VPR.

seasons. Within 2–3 km above the BB, VPRs during all four seasons reveal a quick decrease of reflectivity with increasing height, indicating that stratiform precipitation has a fast rate of ice–snow aggregation. The change of reflectivity is normally $3\text{--}7 \text{ dB km}^{-1}$ and increases in VPRs with heavier precipitation. From a height of 2–3 km above the BB to storm top, the stratiform VPRs generally have weak reflectivity ($<20 \text{ dBZ}$), a small change with height, and thus slow aggregation rates having little contribution to surface rainfall.

Figure 5 shows the characteristics of VPRs for convective precipitation. Much different from stratiform VPRs, convective VPRs have higher storm tops, a deeper range of intensification, and larger reflectivity values for the same rainfall rate measured on the surface. The distinct feature of convective VPRs is their monotonic increase of reflectivity from the storm top to the surface with a few exceptions in very weak convection. Their increasing rates are not as large as in the fast ice–snow aggregation region of stratiform VPRs.

According to the mean standard deviation curves (dashed lines in right side of figures), VPRs with similar surface rain intensities have a small variation below freezing level and larger variation (6 dB) above the freezing level. This result indicates that convective rain with similar intensity tends to have a similar DSD at low levels (e.g., $<2 \text{ km}$) but have larger variations in DSD or particle size distribution (PSD) at high levels (e.g., $>4 \text{ km}$), which can be attributed to the difference in the intensity and the depth of convection. The depth of convective echoes in winter is apparently smaller than with the other three seasons. The standard deviation values above the freezing level are a little smaller for winter ($\sim 4.5 \text{ dB}$) than for the other seasons ($\sim 6 \text{ dB}$). Generally, spring and autumn VPRs have very similar vertical features, except the freezing level is a little higher in autumn. At the height close to the freezing level, there is no notable difference between seasons for mean VPRs with the same surface rainfall rate. From the freezing level to the surface, convective VPRs generally increase in reflectivity though the increase rate is

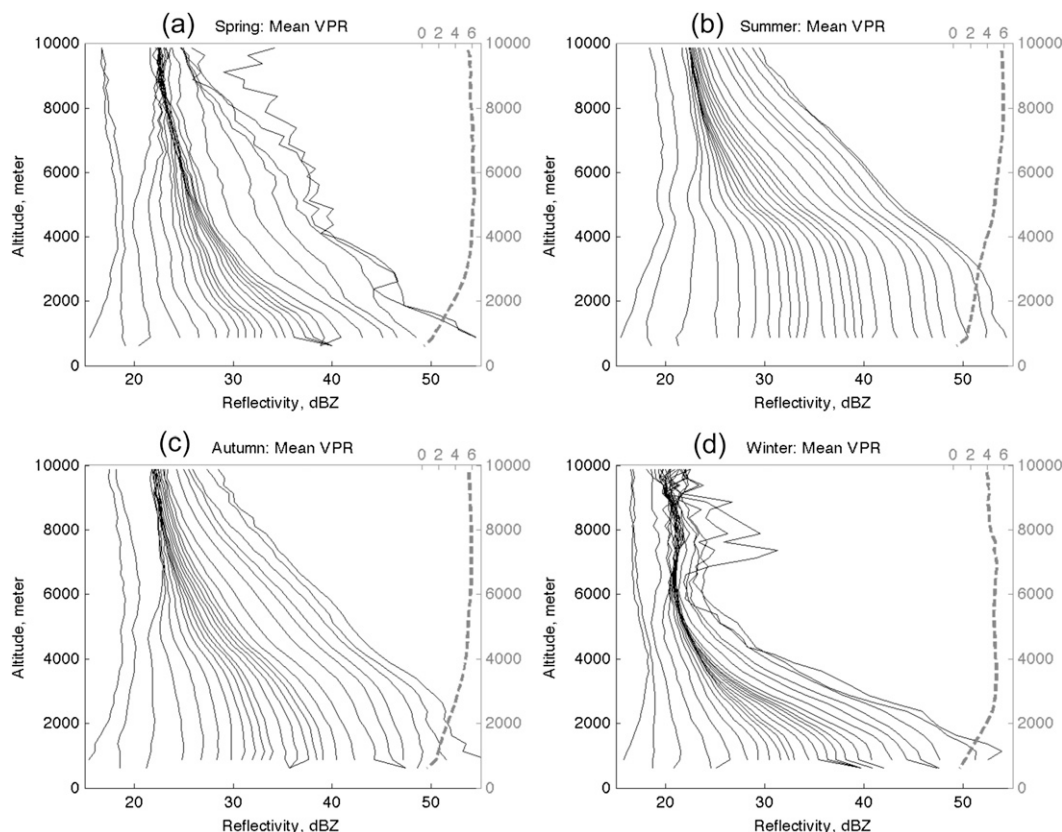


FIG. 5. As in Fig. 4, but for convective precipitation.

small ($<1 \text{ dB km}^{-1}$). On the other hand, some of the stratiform VPRs (e.g., Fig. 4a) show a trend of decreasing reflectivity below the BB, implying that evaporation plays a larger role in reducing surface rainfall rates.

Figure 6 shows the characteristics of VPRs classified as stratiform maybe precipitation. As shown in Fig. 3, this type of precipitation accounts for a majority of PR observations. Figure 6 reveals VPR shapes that are generally similar to those in Fig. 4, except the BB feature is not as notable. Also, some VPRs show features more common to convection such as the monotonic increase of reflectivity from storm top to surface. It is worth noting that the majority of this type of precipitation has a maximum reflectivity of less than 30 dBZ (Fig. 3) and that their surface rainfall rates are less than 2.5 mm h^{-1} . Therefore, the VPR characteristics in Fig. 6 are mainly for weak stratiform echoes, and it is reasonable that the BB feature is not as apparent.

b. Height of storm

It is speculated that storms with higher tops produce more precipitation at the surface given the same precipitation type (Fu et al. 2006). The height of storm is

mainly associated with the intensity of updrafts. It might also be affected by the terrain. TRMM 2A23 algorithm includes one product indicating the height of storm top above mean sea level. Figure 7 shows the spatial distribution of the median height of storm top from TRMM data in the analysis region. The height of storm, as well as other height values used in this study, is evaluated with respect to mean sea level. The height of storm shows the obvious trend of increasing over the higher terrain, especially in spring and winter months. The terrain effect causes a 1–1.5-km difference between the southwest and northeast regions. The terrain effect being less evident in summer and autumn months suggests that the higher the storm top, the less effect from the underlying terrain. Low storm heights (about 3 km) are observed in the southwestern region in winter and spring. Storm top heights in summer are generally 2–4 km higher than the ones in the other seasons. Storms in autumn have higher top heights than in spring. The height of storm has some statistical correlation with surface rainfall rate and maximum reflectivity in the vertical profile (not shown). The degree of correlation depends on the precipitation type and the cold–warm season.

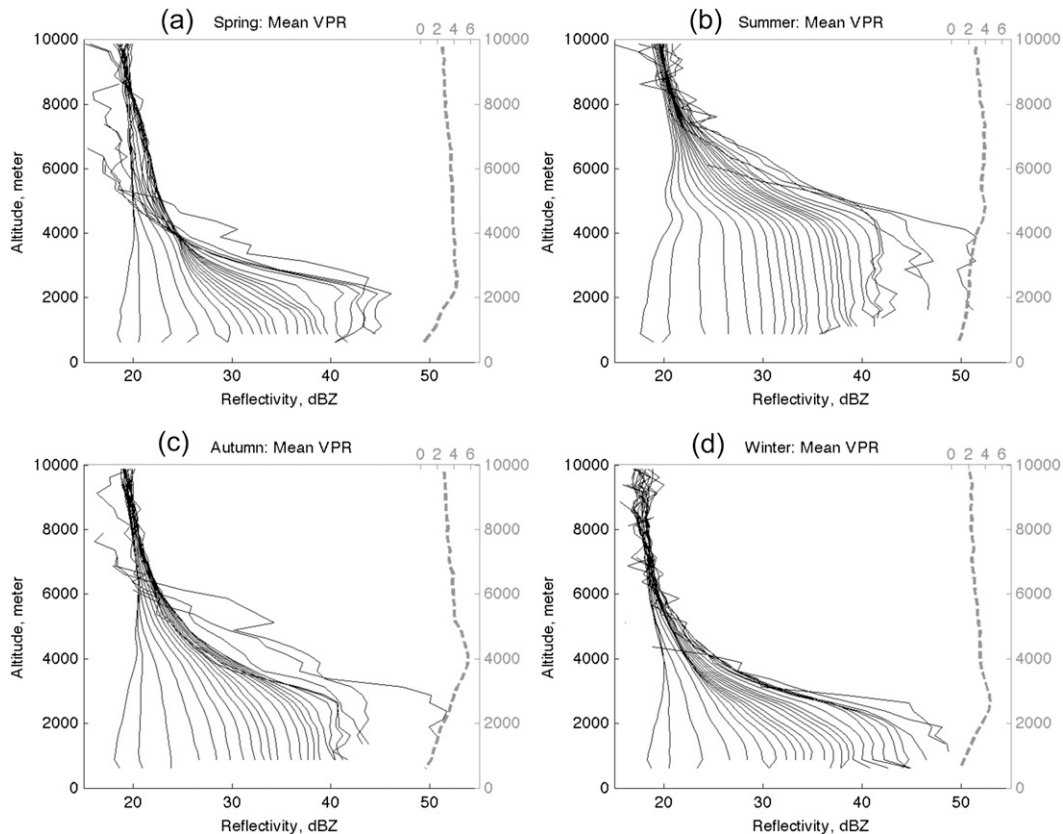


FIG. 6. As in Fig. 4, but for stratiform maybe precipitation.

c. Heights of bright band

The presence of a melting layer is one of the major factors that increase the uncertainty of rainfall estimation

from ground-based radar measurements. Knowledge of BB heights (e.g., heights of freezing level, BB peak and bottom) would help interpreting how much the ground radar beam intercepts or overshoots a melting layer for

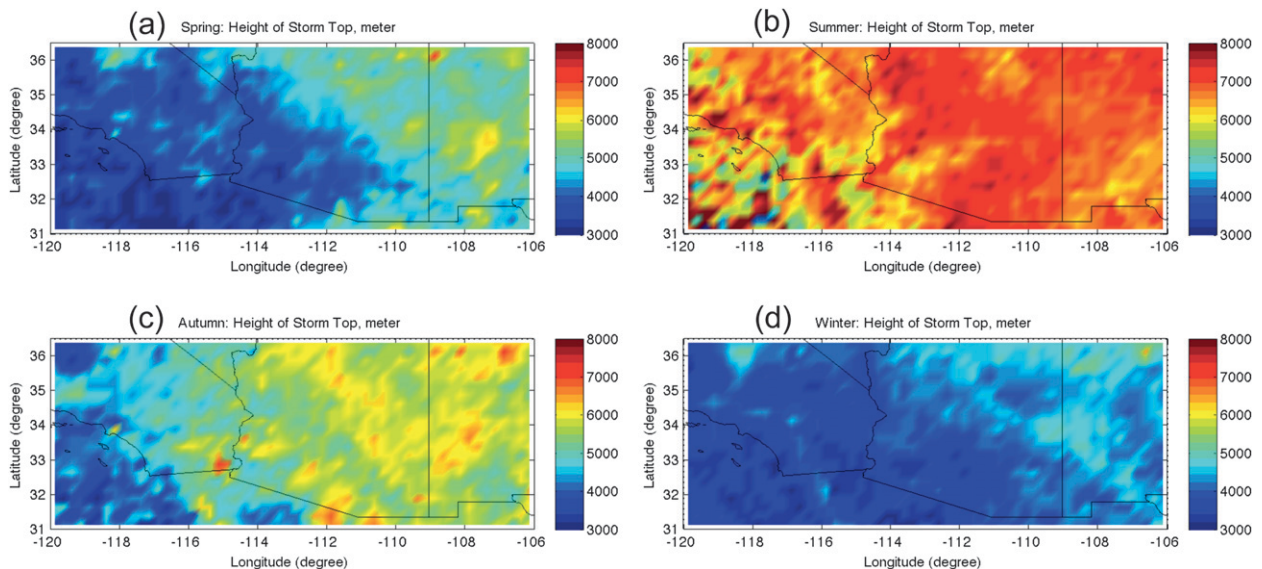


FIG. 7. Seasonal and spatial variation of the storm height: (a) spring, (b) summer, (c) autumn, and (d) winter. The spatial resolution is $0.25^\circ \times 0.25^\circ$.

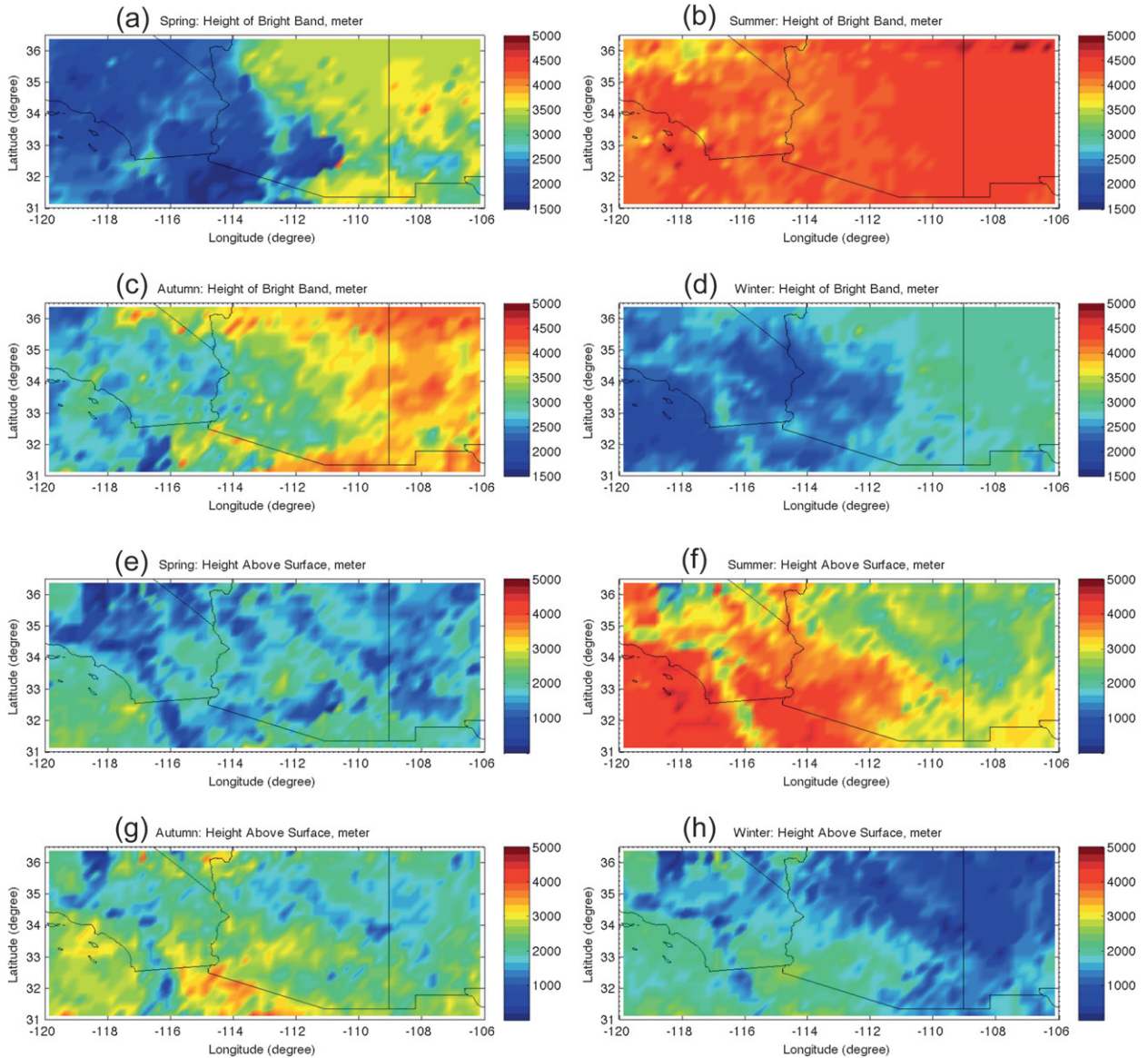


FIG. 8. Seasonal and spatial variation of the height of brightband peak: the absolute height above sea level for (a) spring, (b) summer, (c) autumn, and (d) winter; (e)–(h) the height of brightband peak above surface (i.e., excluding terrain altitude) for the four seasons. The spatial resolution is $0.25^\circ \times 0.25^\circ$.

a given elevation angle at a specific range. Figure 8 shows the seasonal and spatial distribution of the height of peak reflectivity in the melting layer (hereinafter we regard the height of BB peak as a representative height of BB). In general, the height of BB is associated with the ambient temperature, and the 0°C level (not shown) can roughly determine the height of BB. As for the height of BB above the mean sea level shown in Figs. 8a–d, summer has the highest BB that is about 4.5 km for most of the region. The season with the second highest BB is autumn, and the BB in autumn apparently shows more spatial variations of height than in summer. The height of BB is

normally low during the cool season (winter) because of the low height of 0°C . It is noted that in most areas of southern California and southwest Arizona the BB is even lower in spring than in winter. This might be attributed to the cold air that comes from the Pacific Ocean in spring more than in winter. The terrain effect is clearly shown in Figs. 8a–d for all four seasons, although summer appears to have less spatial variations with the terrain altitude. The melting-layer height tends to coincide with the increase in terrain altitude from southwest to northeast in the analysis region. The terrain effect is most evident in spring, and the difference (1500–2000 m) in

terrain from the low deserts in southwest Arizona to the higher mountains to the northeast is of the same order as the height of the BB. In summer, because the melting layer is normally several kilometers above the surface, the terrain effect decreases with increasing the height of BB. These results support the presumption that vertical drafts caused by orographic effects and surface heating by the underlying terrain apparently alter the vertical structure of storms.

Figures 8e–h show the height of BB above the surface, that is, terrain altitude is subtracted from the heights shown in Figs. 8a–d. The BB tends to be closer to the surface with increasing terrain altitude from southwest to northeast in the analysis region. This trend is more apparent in the summer. The BB is 4–4.5 km above the surface in the costal area and southwest Arizona. The height of BB decreases below 2 km in western New Mexico, where the altitude is about 2.5 km. This trend in spring is not as apparent as in the other three seasons. The height of BB above the surface in most of the region in spring varies within a small range (of 1000 m), and the BB height difference is small between high and low terrains. It is also worth noting that the height of BB in spring and winter is generally low (<2 km above the surface). In some areas (e.g., eastern Arizona and west New Mexico) in winter, the BB is even lower than 1000 m. The BB being close to the surface leads to a short depth of the raining region in the VPR, and ground radars' measurement of rainfall is more susceptible to BB contamination or ground clutter.

d. Low-level VPR slope

The VPR from the freezing level to the surface is of most interest to rainfall estimation using ground radar. Knowledge of the rate of increase or decrease of reflectivity at low levels would be helpful to improve surface rainfall estimates. Generally speaking, if only the precipitation physics are involved (without the contribution from sampling issues), the intensification of reflectivity below the freezing level is likely attributed to accretion or collision of raindrops, and weakening is due to evaporation or the breakup of raindrops. As shown by the conceptual diagram of a stratiform VPR in Fig. 9, a linear slope model is utilized to quantify the increase or decrease of the VPR from the BB bottom to the surface (raining region). A linear regression is used to calculate the VPR slope using PR data. A positive slope means there is a reduction in reflectivity going down. The uncertainty of fitting may increase if data points are few for the fitting. As Figs. 8e,h show, in spring and winter the BB is quite close to the surface. Available data points for the raining region of VPR are usually not sufficient (e.g., less than 4), resulting in a relatively large

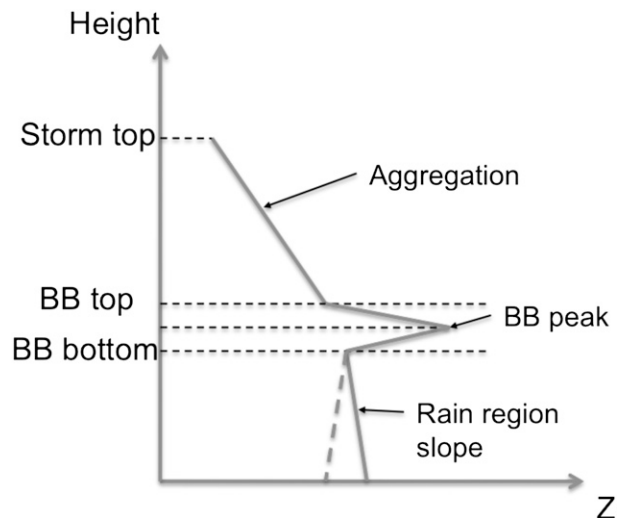


FIG. 9. A conceptual diagram of stratiform VPR. The thick dashed line, which means a positive VPR slope, indicates the decrease of reflectivity from BB bottom to surface. The solid line from BB bottom to surface means a negative VPR slope.

fitting error and therefore inconclusive statistics. Consequently, the discussion of VPR slope in the raining region in spring and winter is not included in this paper.

Figure 10 presents summer and autumn maps of VPR slope over the analysis domain for stratiform, stratiform maybe, and convective precipitation, respectively. It is apparent that stratiform and stratiform maybe precipitation generally has positive slope values. This result supports the presumption that raindrop sizes are reduced, most likely through evaporation, in the raining region below the bottom of BB. There are many factors that could contribute to a faster evaporation, for example, more (or less) small (or large) raindrops, relatively drier ambient conditions, and higher ambient temperature. The impact of evaporation on the radar observation at low levels has been investigated by Kumjian and Ryzhkov (2010). Their results have demonstrated that the potential reduction (several decibels) of VPRs in the raining region could be related to the evaporation. VPR slopes in summer and autumn (Figs. 10a,b) generally have a small value (<2 dB km⁻¹) except some areas, for example, the southeast California in autumn where the VPR slope is mainly 2–4 dB km⁻¹ (Fig. 10a). On the other hand, convective precipitation is quite distinct from stratiform precipitation in that the slope values are generally negative (Fig. 10c). This indicates that reflectivity intensification, instead of reduction, prevails at low levels of convective VPRs. The intensification of reflectivity may be attributed to the change in rain microphysics. Convection generally has stronger updrafts, which enhance collision or coalescence

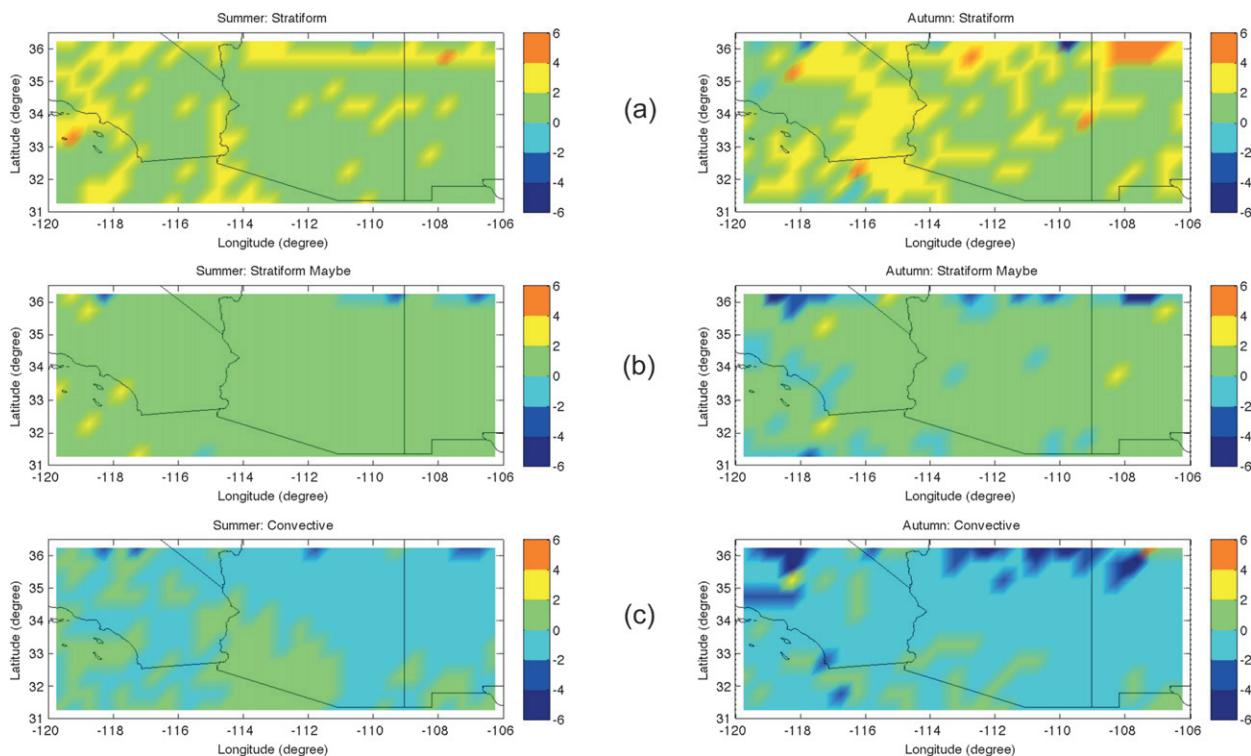


FIG. 10. Seasonal and spatial variation of the VPR slope of raining region: (a) stratiform, (b) stratiform maybe, and (c) convective precipitation for (left) summer and (right) autumn. The spatial resolution is $0.5^\circ \times 0.5^\circ$.

of raindrops at low levels. Compared to stratiform precipitation, the moister environment in convection also reduces the evaporation rate and enables more growth of raindrops. Therefore, the VPR slope tends to be negative in convective precipitation though the slope value is normally small (within -2 dB km^{-1}). An exception is clearly seen in southwest Arizona in summer (Fig. 10c), where VPR rain slopes are positive. Very low relative humidity values in the boundary layer in this dry, desert region likely enhance evaporation rates and result in the weakly positive subcloud slopes. In spite of this exception, the terrain effect on the VPR slope seems weak according to Fig. 10.

Figure 11 investigates the terrain effects on the change of mean slope of VPRs in summer and autumn. For stratiform (or stratiform maybe) precipitation, the effect of terrain appears negligible except for a slight increase in positive slopes for very light rainfall rates (e.g., $<2.5 \text{ mm h}^{-1}$) in higher terrain. The terrain effect is more evident for convective precipitation. There is generally less weakening or greater intensification of reflectivity for rain region in higher terrain, especially for rainfall rates of greater than 4 mm h^{-1} . This result supports the prior inference about stronger updrafts enhancing low-level growth because of turbulence and

collision-coalescence. In higher terrain, surface heating may have a more direct impact on updraft strength because of closer proximity of the surface to cloud base.

The study of Kumjian and Ryzhkov (2010) implies that the evolution of DSD, which results in different rain intensities, may also impact the reduction/intensification of VPR in the raining region. Figure 11 quantifies the change of the VPR rain slopes for VPRs with different surface rainfall rates. Very light rainfall rates ($<2.5 \text{ mm h}^{-1}$) from stratiform clouds are associated with higher slope values than with moderate or heavy rain. Apparently, there are relatively drier ambient conditions with the lightest stratiform rainfall, which enables significant evaporation rates in the boundary layer. The rain slope with stratiform precipitation generally decreases with higher surface rainfall rates, but the VPR slopes remain positive. This trend can be attributed to increasingly moist environments associated with higher rainfall rates that tend to decrease the impact of evaporation. While stratiform precipitation is nominally associated with reductions of various magnitudes in reflectivity as rain droplets fall, convective storms are evaporation dominated for rainfall rates of less than 5 mm h^{-1} , but switch to growth dominated for rainfall rates of more than 18 mm h^{-1} . The trend of more negative rain slopes

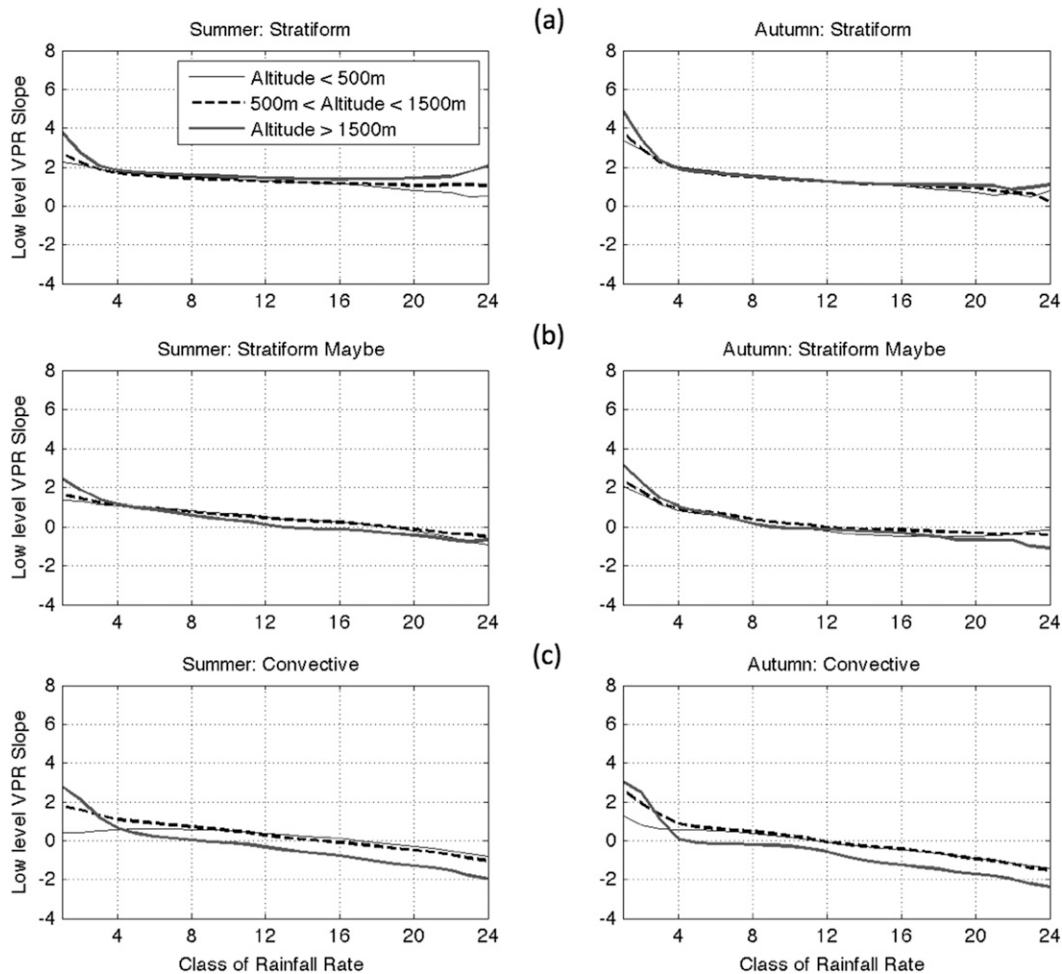


FIG. 11. The effect of terrain's altitude on the low-level VPR slope with different rainfall rates for (a) stratiform, (b) stratiform maybe, and (c) convective precipitation for (left) summer and (right) autumn. The 24 classes of rainfall rate denote 0.4, 0.6, 1.0, 1.5, 2.0, 2.5, 3.0, 3.5, 4.0, 4.5, 5.0, 6.0, 7.0, 8.0, 9.0, 10.0, 12.0, 15.0, 20.0, 25.0, 30.0, 40.0, 60.0, and 80.0 mm h^{-1} , respectively. VPRs used for calculation of each class have the near-surface rainfall rate variation of $\pm 10\%$. Solid lines represent the median value of the VPR slope.

with increasing rainfall rates supports the notion that higher rainfall rates are associated with stronger updrafts, enhanced low-level growth by collision-coalescence, and weaker evaporation rates due to moister environments.

4. Discussion

The statistical quantification of VPR characteristics given in section 3 improves our understanding of the vertical structures of storms in the analysis region and provides for inferences of dominant microphysical processes. Rainfall estimation using NEXRAD radars in the Intermountain West is quite challenging because of beam blockages and limited visibility at low levels. This space-based VPR analysis provides unique insights for VPR correction methods. If a spatially and temporally

representative VPR is known for the different precipitation types, then surface rainfall can be much better estimated with ground radar observations, even for situations where the beam intercepts or overshoots the melting layer. Figure 12 provides representative mean VPRs for stratiform precipitation that have been normalized by reflectivity at a reference height. The horizontal axis represents the ratio of reflectivity (dBZ) to the reference value observed 1 km below the height of the BB peak. Light precipitation has a larger VPR ratio within the melting layer and in the ice region above. This result suggests weaker stratiform precipitation is associated with lower aggregation rates of ice-snow particles above the freezing level and its relatively stronger BB signal may cause further contamination when estimating surface rainfall rates. In addition, the smaller ratios

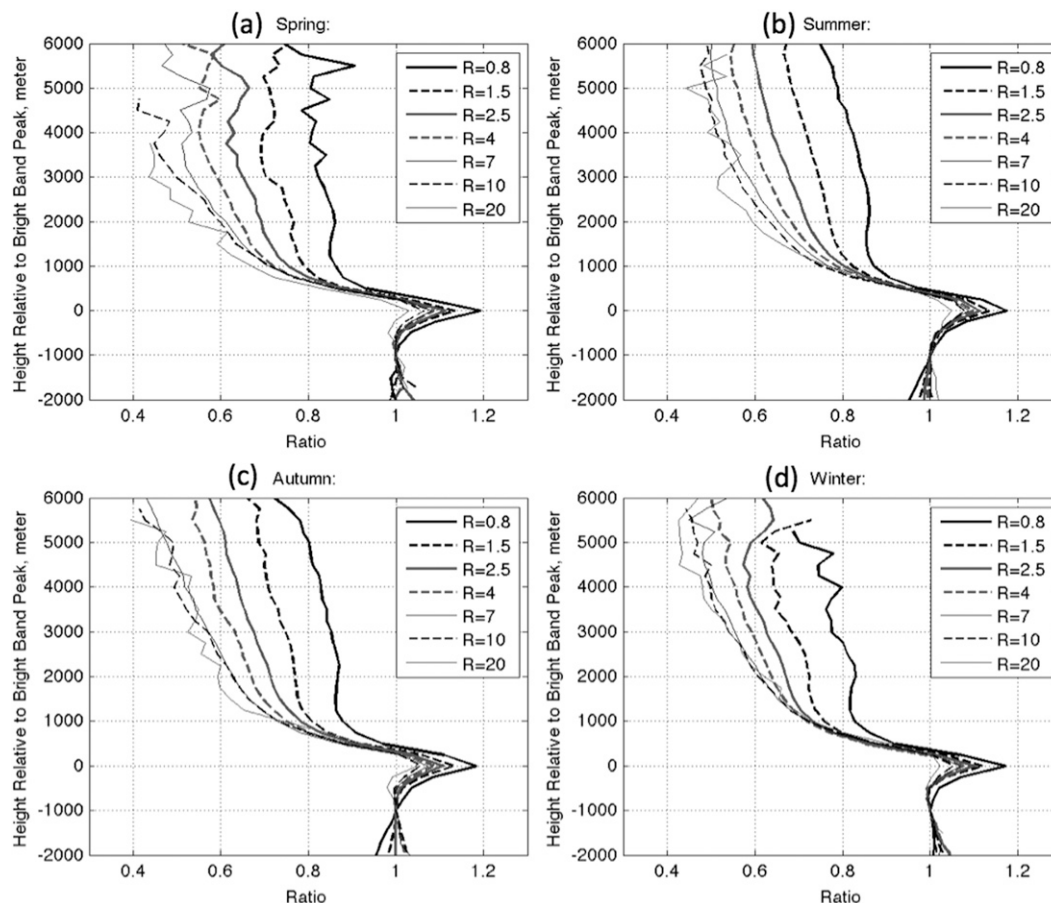


FIG. 12. Normalized VPR shape for stratiform precipitation with different rainfall rates for (a)–(d) the four seasons.

noted below the reference height with light stratiform precipitation indicates that evaporation rates are more influential on the rain slope, as previously discussed. For stratiform precipitation with rainfall rates of greater than 7 mm h^{-1} , VPR ratios in the ice–snow aggregation region and melting layer are very similar, suggesting that the VPR structures for heavy stratiform rain tend to be less variable and are thus more predictable. Seasonal variations of stratiform VPRs for a given rainfall rate class are also slight and largely negligible. These results are encouraging for VPR correction methodologies for ground-based radars in that the local VPR, when normalized and segregated to the reference value below the BB, appear to be consistent from season-to-season for stratiform precipitation. When the PR-derived VPRs in Fig. 12 are used for the ground radar reflectivity correction, a vertical smoothing needs to be considered to account for the change of radar sampling volume at different radar ranges. It is also worth noting that polarimetric radar has good potential to identify the vertical structure of storms as well as the bright band

(Matrosov et al. 2007). The VPR correction can be further improved for dual-polarization upgraded NEXRAD because polarimetric ground radar can provide more information of local VPR, which helps reduce the uncertainty of PR-derived climatological VPR.

All the VPR characteristics in prior analyses are derived from Ku-band TRMM PR observations. The TRMM PR observation can be degraded by precipitation attenuation, which can be quite severe for Ku-band radar. The attenuation, if not well corrected, might affect the previous analysis results. In this study, we have ignored this issue and rely on the attenuation-corrected radar reflectivity and corresponding rainfall estimation, which have been provided by TRMM science team. Thus, results and conclusions from our study are conditioned on the validity of those products. In addition, the Ku-band VPR shape cannot be used directly for S-band NEXRAD observations. The conversion of reflectivity from Ku band to S band is another issue that needs to be taken into consideration when using the PR-based climatological VPR analyses presented herein

to correct NMQ-Q2-based precipitation estimates. This conversion requires knowledge of the scattering properties of hydrometeors for the two different radar frequencies. It also requires appropriate assumptions of microphysical processes during the transition from ice to liquid phase. Nonetheless, the PR-based climatology should provide guidance on the proper VPR correction approaches needed to improve surface precipitation estimates using ground radar observations in complex terrain.

A detailed discussion of the mechanics of using the climatological VPR information into a correction approach is beyond the scope of this study. However, we supply some general directions on how the climatological VPR information can be used to augment ground radar-based rainfall estimates. The VPR shapes (normalized reflectivity) shown in Fig. 12 are representative Ku-band VPR shapes for different rainfall intensities. Those Ku-band shapes will be converted to similar shapes, but for S band using either a physics-based model (Kirstetter et al. 2010) or empirical methods (to be studied). Given a specific location, the climatological VPRs will be adjusted by considering the effects of ground radar sampling geometry such as beam broadening. Then, the adjusted VPR shapes will be combined with the ground radar reflectivity (normally observed at high levels in mountainous regions) to estimate the reflectivity in the rain region (at low levels). It is noted that the application of the climatological VPR needs to consider which VPR shape (for a specific rainfall rate) should be utilized. This step will require VPR matching using reflectivity observations aloft, and may even consider ensemble approaches. Ultimately, the ground radar reflectivity observed at a height above—within the bright band can be related to the surface reflectivity and used to estimate the surface rainfall rates, even when radar observations near the surface are blocked by the mountains.

5. Conclusions

This study investigates the statistical seasonal and spatial characteristics of the vertical structure of precipitation in the region of southern California, Arizona, and western New Mexico through the use of 11+ years of TRMM PR observations. The findings are briefly summarized as follows.

- 1) The most significant factor defining the characteristics of VPRs is precipitation type. Stratiform and convective storms, which are controlled by different microphysical and thermodynamical processes, have distinct VPR shapes in the transitions from the ice to the raining region. More than 90% of stratiform

echoes in the analysis domain had column-maximum reflectivity of less than 34 dBZ whereas more than 40% of convective storms had column-maximum reflectivity of greater than 34 dBZ.

- 2) The intensity of surface rainfall rates was found to strongly influence the shape of VPRs. Profiles associated with moderate and heavy surface rainfall rates in stratiform precipitation had much greater reductions in reflectivity above the melting layer than with lighter rainfall rates. This steep slope indicates the ice/snow aggregation rates are apparently much greater in stratiform precipitation with moderate and heavy surface rainfall rates.
- 3) The characteristics of VPRs had a seasonal dependence with strong similarities between the spring and autumn months. In general, storm-top and bright-band heights increased during the summer months.
- 4) The spatial variation of VPR characteristics suggests that the underlying terrain has an impact on the vertical structure. Storm-top heights were found to vary with the underlying terrain elevations, and convective echoes had less weakening or greater intensification of reflectivity for raining regions in higher terrain, especially for rainfall rates of more than 4 mm h^{-1} . The height of the brightband peak was also found to vary with the terrain. Apparently, the heating of the surface and orographically induced updrafts impact the VPR shapes.
- 5) The slope of the VPR below the bright band in the raining region was positive with stratiform precipitation suggesting reflectivity decreased downward because of evaporation. Slopes became more negative with convective echoes and with increasing surface rainfall rates. Apparently, the strength of updrafts influences collision-coalescence rates and overwhelms evaporative effects on the low-level VPR slope. Boundary layer relative humidity is another factor influencing evaporation rates and VPR slopes in the raining regions.
- 6) Statistical analysis of VPR characteristics in the analysis region suggests that a representative VPR model for a given precipitation type can be built based on the integration of normalized VPR shape. The shape of the VPR was found to be sensitive to rain intensity and the height of the bright band, the latter of which varies seasonally and spatially with an underlying terrain influence. This representative VPR can be used to correct surface precipitation estimates in regions where ground-based NEXRAD radar has limited visibility at low levels in complex terrain.

A logical extension of this work is the development of a VPR correction method to NEXRAD-based observations

to be implemented and tested in the study region. There are still many issues that must be addressed, such as VPR modeling using ground and spaceborne measurements combined, estimating the spatiotemporal representativeness and resultant uncertainty in surface precipitation estimates, and the conversion from Ku-band to S-band reflectivity with different hydrometeor types. These issues will be addressed and reported on in future studies.

Acknowledgments. This work was supported by NASA Grant NNX11AL78G with the title of “Incorporating NASA Spaceborne Precipitation Research Products into National Mosaic QPE Real-time System for Improved Short-term Weather Prediction at Colorado Basin River Forecast Center” and the NOAA Multi-Function Phased-Array Radar Project administered by the Atmospheric Radar Research Center at the University of Oklahoma. We appreciate scientists and engineers from NASA, who have made the TRMM PR data available.

REFERENCES

- Awaka, J., T. Iguchi, and K. Okamoto, 2007: Rain type classification algorithm. *Measuring Precipitation from Space—EURAINSAT and the Future*, V. Levizzani, P. Bauer, and F. J. Turk, Eds., Springer, 213–224.
- , —, and —, 2009: TRMM PR standard algorithm 2A23 and its performance on bright band detection. *J. Meteor. Soc. Japan*, **87A**, 31–57.
- Bellon, A., G.-W. Lee, and I. Zawadzki, 2005: Error statistics of VPR corrections in stratiform precipitation. *J. Appl. Meteor.*, **44**, 998–1015.
- Fabry, F., and I. Zawadzki, 1995: Long-term radar observations of the melting layer of precipitation and their interpretation. *J. Atmos. Sci.*, **52**, 838–851.
- Fu, Y., J. Feng, H. Zhu, R. Li, and D. Liu, 2006: Precipitation structures of a thermal convective system happened in the central western subtropical Pacific anticyclone. *Acta Meteor. Sin.*, **20**, 232–243.
- Gabella, M., E. Morin, and R. Notarpietro, 2011: Using TRMM spaceborne radar as a reference for compensating ground-based radar range degradation: Methodology verification based on rain gauges in Israel. *J. Geophys. Res.*, **116**, D02114, doi:10.1029/2010JD014496.
- Geerts, B., and T. Dejene, 2005: Regional and diurnal variability of the vertical structure of precipitation systems in Africa based on spaceborne radar data. *J. Climate*, **18**, 893–916.
- Germann, U., and J. Joss, 2002: Mesobeta profiles to extrapolate radar precipitation measurements above the Alps to the ground level. *J. Appl. Meteor.*, **41**, 542–557.
- Hirose, M., and K. Nakamura, 2002: Spatial and seasonal variation of rain profiles over Asia observed by spaceborne precipitation radar. *J. Climate*, **15**, 3443–3458.
- , and —, 2004: Spatiotemporal variation of the vertical gradient of rainfall rate observed by the TRMM precipitation radar. *J. Climate*, **17**, 3378–3397.
- Iguchi, T., T. Kozu, R. Meneghini, J. Awaka, and K. Okamoto, 2000: Rain-profiling algorithm for the TRMM precipitation radar. *J. Appl. Meteor.*, **39**, 2038–2052.
- , —, J. Kwiatkowski, R. Meneghini, J. Awaka, and K. Okamoto, 2009: Uncertainties in the rain profiling algorithm for the TRMM precipitation radar. *J. Meteor. Soc. Japan*, **87A**, 1–30.
- Kirstetter, P.-E., H. Andrieu, G. Delrieu, and B. Boudevillain, 2010: Identification of vertical profiles of reflectivity for correction of volumetric radar data using rainfall classification. *J. Appl. Meteor. Climatol.*, **49**, 2167–2180.
- Kitchen, M., R. Brown, and A. G. Davies, 1994: Real-time correction of weather radar data for the effects of bright band, range and orographic growth in widespread precipitation. *Quart. J. Roy. Meteor. Soc.*, **120**, 1231–1254.
- Kozu, T., and Coauthors, 2001: Development of precipitation radar onboard the Tropical Rainfall Measuring Mission (TRMM) satellite. *IEEE Trans. Geosci. Remote Sens.*, **39**, 102–116, doi:10.1109/36.898669.
- Kumjian, M. R., and A. V. Ryzhkov, 2010: The impact of evaporation on polarimetric characteristics of rain: Theoretical model and practical implications. *J. Appl. Meteor. Climatol.*, **49**, 1247–1267.
- Kummerow, C., and Coauthors, 2000: The status of the Tropical Rainfall Measuring Mission (TRMM) after two years in orbit. *J. Appl. Meteor.*, **39**, 1965–1982.
- Lakshmanan, V., A. Fritz, T. Smith, K. Hondl, and G. Stumpf, 2007: An automated technique to quality control radar reflectivity data. *J. Appl. Meteor. Climatol.*, **46**, 288–305.
- Maddox, R. A., J. Zhang, J. J. Gourley, and K. W. Howard, 2002: Weather radar coverage over the contiguous United States. *Weather Forecasting*, **17**, 927–934.
- Matrosov, S. Y., K. A. Clark, and D. E. Kingsmill, 2007: A polarimetric radar approach to identify rain, melting-layer, and snow regions for applying corrections to vertical profiles of reflectivity. *J. Appl. Meteor. Climatol.*, **46**, 154–166.
- Meneghini, R., T. Iguchi, T. Kozu, L. Liao, O. Ken'ichi, J. A. Jones, and J. Kwiatkowski, 2000: Use of the surface reference technique for path attenuation estimates from the TRMM precipitation radar. *J. Appl. Meteor.*, **39**, 2053–2070.
- , J. A. Jones, T. Iguchi, K. Okamoto, and J. Kwiatkowski, 2004: A hybrid surface reference technique and its application to the TRMM precipitation radar. *J. Atmos. Oceanic Technol.*, **21**, 1645–1658.
- Schumacher, C., and R. A. Houze Jr., 2003: The TRMM precipitation radar's view of shallow, isolated rain. *J. Appl. Meteor.*, **42**, 1519–1524.
- Seto, S., and T. Iguchi, 2007: Rainfall-induced changes in actual surface backscattering cross sections and effects on rain-rate estimates by spaceborne precipitation radar. *J. Atmos. Oceanic Technol.*, **24**, 1693–1709.
- Shin, D., G. R. North, and K. P. Bowman, 2000: A summary of reflectivity profiles from the first year of TRMM radar data. *J. Climate*, **13**, 4072–4086.
- Steiner, M., R. A. Houze Jr., and S. E. Yuter, 1995: Climatological characterization of three-dimensional storm structure from operational radar and rain gauge data. *J. Appl. Meteor.*, **34**, 1978–2007.
- Takahashi, N., and T. Iguchi, 2004: Estimation and correction of beam mismatch of the precipitation radar after an orbit boost of the Tropical Rainfall Measuring Mission satellite. *IEEE Trans. Geosci. Remote Sens.*, **42**, 2362–2369.
- TRMM Precipitation Radar Team, 2011: Tropical Rainfall Measuring Mission (TRMM) precipitation radar algorithm: Instruction manual for version 7. Japan Aerospace Exploration

- Agency, Tokyo, Japan, 170 pp. [Available online at http://www.eorc.jaxa.jp/TRMM/documents/PR_algorithm_product_information/pr_manual/PR_Instruction_Manual_V7_L1.pdf.]
- Vasiloff, S., and Coauthors, 2007: Improving QPE and very short term QPF: An initiative for a community-wide integrated approach. *Bull. Amer. Meteor. Soc.*, **88**, 1899–1911.
- Vignal, B., G. Galli, J. Joss, and U. Germann, 2000: Three methods to determine profiles of reflectivity from volumetric radar data to correct precipitation estimates. *J. Appl. Meteor.*, **39**, 1715–1726.
- Williams, C. R., A. B. White, K. S. Gage, and F. Martin Ralph, 2007: Vertical structure of precipitation and related microphysics observed by NOAA profilers and TRMM during NAME 2004. *J. Climate*, **20**, 1693–1712.
- Zhang, J., and Y. Qi, 2010: A real-time algorithm for the correction of brightband effects in radar-derived QPE. *J. Hydrometeor.*, **11**, 1157–1171.
- , K. Howard, and J. J. Gourley, 2005: Constructing three-dimensional multiple radar reflectivity mosaics: Examples of convective storms and stratiform rain echoes. *J. Atmos. Oceanic Technol.*, **22**, 30–42.
- , and Coauthors, 2011: National Mosaic and Multi-sensor QPE (NMQ) system: Description, results, and future plans. *Bull. Amer. Meteor. Soc.*, **92**, 1321–1338.